Gentile, Fabrizio; Casey, Caitlin M.; Akins, Hollis B.; Franco, Maximilien; McKinney, Jed; Berman, Edward; Cooper, Olivia R.; Drakos, Nicole E.; Hirschmann, Michaela; Long, Arianna S.; Magdis, Georgios; Koekemoer, Anton M.; Kokorev, Vasily; Shuntov, Marko; Talia, Margherita; Allen, Natalie; Harish, Santosh; Ilbert, Olivier; McCracken, Henry Joy; Kartaltepe, Jeyhan S.; Liu, Daizhong; Paquereau, Louise; Rhodes, Jason; Rich, Michael R.; Robertson, Brant E.; Toft, Sune; Gozaliasl, Ghassem

Not-so-little Red Dots : Two Massive and Dusty Starbursts at z ~ 5-7 Pushing the Limits of Star Formation Discovered by JWST in the COSMOS-Web Survey

Not-so-little Red Dots: Two Massive and Dusty Starbursts at $z \sim 5$–7 Pushing the Limits of Star Formation Discovered by JWST in the COSMOS-Web Survey

Fabrizio Gentile[1,2], Caitlin M. Casey[3], Hollis B. Akins[3], Maximilien Franco[3], Jed McKinney[3], Edward Berman[4], Olivia R. Cooper[3,22], Nicole E. Drakos[5], Michaela Hirschmann[6,7], Arianna S. Long[3,23], Georgios Magdis[8,9,10], Anton M. Koekemoer[11], Vasily Kokorev[12], Marko Shuntov[8,10], Margherita Talia[1,2], Natalie Allen[8,10], Santosh Harish[13], Olivier Ilbert[14], Henry Joy McCracken[15], Jeyhan S. Kartaltepe[13], Daizhong Liu[16], Louise Paquereau[15], Jason Rhodes[17], Michael R. Rich[18], Brant E. Robertson[19], Sune Toft[8,10], and Ghassem Gozaliasl[20,21]

[1] University of Bologna, Department of Physics and Astronomy (DIFA), Via Gobetti 93/2, I-40129, Bologna, Italy; fabrizio.gentile3@unibo.it
[2] INAF—Osservatorio di Astrofisica e Scienza dello Spazio, via Gobetti 93/3-40129, Bologna, Italy
[3] The University of Texas at Austin, 2515 Speedway Boulevard Stop C1400, Austin, TX 78712, USA
[4] Department of Physics, Northeastern University, 360 Huntington Ave., Boston, MA, USA
[5] Department of Physics and Astronomy, University of Hawaii, Hilo, 200 W Kawili St., Hilo, HI 96720, USA
[6] Institute of Physics, GalSpec, Ecole Polytechnique Federale de Lausanne, Observatoire de Sauverny, Chemin Pegasi 51, 1290 Versoix, Switzerland
[7] INAF, Astronomical Observatory of Trieste, Via Tiepolo 11, 34131 Trieste, Italy
[8] Cosmic Dawn Center (DAWN), Denmark
[9] DTU-Space, Technical University of Denmark, Elektrovej 327, 2800, Kgs. Lyngby, Denmark
[10] Niels Bohr Institute, University of Copenhagen, Jagtvej 128, DK-2200, Copenhagen, Denmark
[11] Space Telescope Science Institute, 3700 San Martin Dr., Baltimore, MD 21218, USA
[12] Kapteyn Astronomical Institute, University of Groningen, PO Box 800, 9700 AV Groningen, The Netherlands
[13] Laboratory for Multiwavelength Astrophysics, School of Physics and Astronomy, Rochester Institute of Technology, 84 Lomb Memorial Dr., Rochester, NY 14623, USA
[14] Aix Marseille Univ, CNRS, CNES, LAM, Marseille, France
[15] Institut d'Astrophysique de Paris, UMR 7095, CNRS, and Sorbonne Université, 98 bis boulevard Arago, F-75014 Paris, France
[16] Purple Mountain Observatory, Chinese Academy of Sciences, 10 Yuanhua Road, Nanjing 210023, People's Republic of China
[17] Jet Propulsion Laboratory, California Institute of Technology, 4800 Oak Grove Dr., Pasadena, CA 91001, USA
[18] Department of Physics and Astronomy, UCLA, PAB 430 Portola Plaza, Box 951547, Los Angeles, CA 90095-1547, USA
[19] Department of Astronomy and Astrophysics, University of California, Santa Cruz, 1156 High St., Santa Cruz, CA 95064, USA
[20] Department of Computer Science, Aalto University, PO Box 15400, Espoo, FI-00 076, Finland
[21] Department of Physics, P.O. Box 64, 00014 University of Helsinki, Finland

Abstract

We present the properties of two candidate massive ($M_\star \sim 10^{11} M_\odot$) and dusty ($A_v > 2.5$ mag) galaxies at $z = 5$–7 in the first 0.28 deg^2 of the COSMOS-Web survey. One object is spectroscopically confirmed at $z_{\rm spec} = 5.051$, while the other has a robust $z_{\rm phot} = 6.7 \pm 0.3$. Thanks to their extremely red colors (F277W–F444W ~ 1.7 mag), these galaxies satisfy the nominal color selection for the widely studied "little red dot" (LRD) population with the exception of their spatially resolved morphologies. The morphology of our targets allows us to conclude that their red continuum is dominated by highly obscured stellar emission and not by reddened nuclear activity. Using a variety of spectral energy distribution fitting tools and star formation histories, we estimate the stellar masses to be $\log(M_\star) = 11.32^{+0.07}_{-0.15} \, M_\odot$ and $\log(M_\star) = 11.2^{+0.1}_{-0.2} \, M_\odot$, respectively, with a red continuum emission dominated by a recent episode of star formation. We then compare their number density to the halo mass function to infer stellar baryon fractions of $\epsilon_\star \sim 0.25$ and $\epsilon_\star \sim 0.5$. Both are significantly higher than what is commonly observed in lower-z galaxies or more dust-obscured galaxies at similar redshifts. With very bright ultra-high-z Lyman-Break Galaxies and some non-AGN-dominated LRDs, such "extended" LRDs represent another population that may require very efficient star formation at early times.

1. Introduction

Since its launch, the James Webb Space Telescope (JWST) has dramatically changed our perspective on the high-z Universe. The discovery of a significant population of highly red and compact sources at $z \gtrsim 5$ ("little red dots"; LRDs henceforth) is puzzling in their origin. These objects have been found in most of the first JWST surveys through their color in the long-wavelength (LW) filters of NIRCam (mainly F277W and F444W; see, e.g., I. Labbé et al. 2023a, 2023b; H. B. Akins et al. 2023; J. Matthee et al. 2024; V. Kokorev et al. 2024; P. G. Pérez-González et al. 2024). These analyses have shown that LRDs are predominately at $z \gtrsim 5$ (with few lower-z analogs; see, e.g., the low fraction of Extremely Red Objects at $z < 5$ reported by G. Barro et al. 2023), are spatially compact, and some have a seemingly decoupled blue spectral energy distribution (SED) rising into the rest-UV (e.g., I. Labbé et al. 2023a, 2023b; V. Kokorev et al. 2024;

P. G. Pérez-González et al. 2024). Moreover, the first spectroscopic follow-ups showed a significant presence of broad emission lines in their spectra, suggesting the presence of active galactic nuclei (AGN) in their cores with a high $M_{BH}/M_\star$ ratio (D. D. Kocevski et al. 2023; L. J. Furtak et al. 2024; J. E. Greene et al. 2024; J. Matthee et al. 2024).

Still unclear is the main physical process responsible for the red continuum: is it highly obscured stellar emission (e.g., I. Labbé et al. 2023a; H. B. Akins et al. 2023; M. Xiao et al. 2023; P. G. Pérez-González et al. 2024; C. C. Williams et al. 2024) or reddened radiation emitted by the AGN (e.g., I. Labbé et al. 2023b; J. E. Greene et al. 2024; V. Kokorev et al. 2024)?

Modeling the SED of these galaxies with stellar-only templates, one can obtain near "Universe-breaking" stellar masses (up to $\sim 10^{11}\ M_\odot$ at $z \sim 8$; see, e.g., I. Labbé et al. 2023a). These values were in tension with the current cosmological model (e.g., M. Boylan-Kolchin 2023), unless (after some downward revisions) we assume that the star formation in the high-z Universe is much more efficient than what is commonly observed at lower-z (see, e.g., M. Xiao et al. 2023). Of course, assuming that the reddened emission comes from an AGN accretion disk lowers the stellar mass estimates, but a new problem arises when the number density of these LRDs is compared with the quasar luminosity function (e.g., X. Shen et al. 2020), as LRDs are 100–1000 times more common, implying an overabundant population of massive black holes at early times (J. E. Greene et al. 2024).

One of the main reasons for the uncertainty about the dominant continuum emission in LRDs is their compactness, not allowing us to completely disentangle the nuclear and stellar contribution. For this reason, in this Letter, we set out to find sources that fulfill the color selection of LRDs but have unambiguously extended morphologies with no embedded point source emission. By virtue of their spatial extent, we can attribute their continuum to stellar origin and—therefore—obtain AGN-unbiased estimation of the stellar masses. In this Letter, we report the discovery of two candidate massive ($M_\star \sim 10^{11}\ M_\odot$) galaxies (one of which already has a spectroscopic redshift from the literature) in the COSMOS-Web survey (C. M. Casey et al. 2023). Section 2 presents the parent sample from which we select our resolved LRD candidates and the photometry available for them in COSMOS-Web. Section 3 describes the SED fitting procedure followed to estimate the photo-z and physical properties, including stellar masses, of our sources, and Section 4 presents a morphological analysis of our sources. Section 5 discusses our results, by placing our galaxies in a cosmological context. Finally, we conclude in Section 6. Throughout this study, we assume a flat ΛCDM cosmology with the parameters reported in Planck Collaboration et al. (2020), a G. Chabrier (2003) initial mass function (IMF), and the AB photometric system (J. B. Oke & J. E. Gunn 1983).

2. Data

2.1. JWST Photometry from COSMOS-Web

The NIRCam and MIRI photometry for our sources comes from the COSMOS-Web survey (GO #1727; PIs: Kartaltepe & Casey; C. M. Casey et al. 2023), a Cycle 1 treasury program consisting of the NIRCam and MIRI imaging of the central region of the COSMOS field (see, e.g., N. Scoville et al. 2007; A. M. Koekemoer et al. 2007). A full description of the survey

design and main scientific goals can be found in C. M. Casey et al. (2023), while a complete discussion about the data reduction will be included in M. Franco et al. (2024, in preparation). In this Letter, we focus on the first data acquired in the COSMOS-Web survey during JWST Cycle 1 in January and April 2023, covering ~ 0.28 deg^2 with NIRCam (i.e., 52% of the total area of the survey).

The space-based photometry in COSMOS is extracted with `sourceXtractor++` (SE++ in the following; E. Bertin et al. 2020; M. Kümmel et al. 2020), a model-based tool for extracting photometry from data sets with different spatial resolution. Detection is conducted on a χ^2-image (A. S. Szalay et al. 1999) generated by coadding the four NIRCam filter maps. A double Sérsic profile (J. L. Sérsic 1963) is fitted to the four NIRCam filter images simultaneously. Further details about the COSMOS-Web catalogs will be included in M. Shuntov & L. Paquereau et al. (2024, in preparation).

By default, SE++ photometric uncertainties do not include Poisson noise from the background (see, e.g., the discussion in H. B. Akins et al. 2023 and C. M. Casey et al. 2024). Therefore, we measure the background noise in empty circular apertures and add it in quadrature to the uncertainties estimated by SE++, following C. M. Casey et al. (2024).

2.2. Initial Sample Selection

The goal of this work is to find spatially resolved sources with analogous colors to the LRDs (e.g., I. Labbé et al. 2023a, 2023b; H. B. Akins et al. 2023; V. Kokorev et al. 2024; P. G. Pérez-González et al. 2024). Therefore, the initial sample selection consists of a color cut to collect all the reddest sources in the survey area. We adopt the same criterion as in G. Barro et al. (2023) and analogous to that employed by H. B. Akins et al. (2023):

$$F277W - F444W > 1.5\ \text{mag}. \qquad (1)$$

To reduce the possible contamination by fake sources and focus only on the robustly detected galaxies, we couple the color cut with three additional criteria:

$$F444W < 27.5\ \text{mag} \qquad (2)$$

$$S/N(F277W) > 2 \qquad (3)$$

$$S/N(F444W) > 4. \qquad (4)$$

We do not include any signal-to-noise ratio (S/N) requirement in F115W and F150W since we expect most of the high-z or highly dust-obscured sources to drop out at these wavelengths. Moreover, the depth of COSMOS-Web in the short-wavelength (SW) filters is slightly shallower than those of other surveys where LRDs have been detected (see, e.g., R. Bezanson et al. 2022; S. L. Finkelstein et al. 2023). Therefore, we do not expect significant emission in these filters even with a similar SED. Moreover, as noted by G. Barro et al. (2023), the inclusion of the additional constraint on the blue colors of LRDs seems to bias the sample toward high-z objects. Without this criterion, we aim to focus on the full redshift distribution of these sources. In addition, H. B. Akins et al. (2024)—also selecting (unresolved) LRDs in the COSMOS-Web survey with the same color cut employed here—showed how this selection can produce a sample of galaxies with properties analogous to those obtained by adding constraints on the blue shape of the

SED. All these criteria produce an initial sample of $\sim$450 sources, after a first vetting to remove imaging artifacts.

This sample includes a large sample of spatially compact LRDs (H. B. Akins et al. 2024). To focus only on the resolved objects, we perform an initial profile fitting on the F444W maps (i.e., those in which we expect our galaxies to have the highest S/N), forcing the modeling with an unresolved point source (in doing so, we employ the empirical point-spread function (PSF) computed on the scientific mosaics through the software PSFEx and the standard routines included in the Astropy library; Astropy Collaboration et al. 2022; E. Bertin 2011). We exclude all galaxies that are well-described as an unresolved point source (i.e., with a reduced $\chi^2 \sim 1$ and no significant residual once subtracted from the unresolved model). The final sample of galaxies consists of 61 objects. The whole sample—including new objects found in the full 0.54 deg^2—will be described in a forthcoming paper (F. Gentile et al. 2024, in preparation), and here we focus on the two unique sources among the 61, selected for being particularly high redshift with high stellar mass estimates (both of which are described in detail below). Both galaxies, which we named ERD-1 and ERD-2 (for "extended red dots"), have F277W–F444W ~ 1.75, just slightly lower than the color cut by H. B. Akins et al. (2023), but still significantly redder than the nominal LRD selection (with F277W–F444W > 1 mag; see, e.g., I. Labbé et al. 2023a; J. E. Greene et al. 2024; P. G. Pérez-González et al. 2024).

2.3. Ancillary Data

We extract additional photometry for our sources, using the wealth of other ground/space imaging in COSMOS. We extract fluxes in fixed circular apertures from the data sets in J. R. Weaver et al. (2022). These include the Subaru data (HyperSuprimeCam Subaru Strategic Program, HSC SSP DR3; H. Aihara et al. 2019), VISTA data (UltraVISTA survey DR5; H. J. McCracken et al. 2012), Spitzer Space Telescope data (Cosmic Dawn Survey; A. Moneti et al. 2022), and Hubble Space Telescope data (A. M. Koekemoer et al. 2007). We use a fixed aperture radius of 1″, well-matched to seeing limits of the ground based-data. For the *Spitzer* data, we only include the photometric point at 3.6 μm as the second channel is superseded by F444W. We calculate aperture corrections by convolving the best-fitting model by SE++ with the IRAC PSF and calculating what fraction of the total flux is missed.

2.4. ALMA Data on ERD-1

ERD-1 has a reported spectroscopic redshift $z_{\rm spec} = 5.051$ in the literature from S. Jin et al. (2019) thanks to an Atacama Large Millimeter/submillimeter Array (ALMA) spectral scan. They find a single line at 95.2 GHz (5.97σ). The lack of other lines identified in the broad frequency range leads to the conclusion the line is CO(5-4). As noted in Section 3, our new JWST photometry is inconsistent with lower redshift explanations (e.g., CO(4 − 3) at $z = 3.84$ or CO(3 − 2) at $z = 2.63$). S. Jin et al. (2019) measure a (sub)millimeter flux density at 3 mm of $S_{\rm 3\,mm} = (0.115 \pm 0.008)$ mJy after removing the spectral line. ERD-1 is also detected at $\lambda = 2$ mm in the Ex-MORA survey (A. S. Long et al. 2024, in preparation), the extended version of the original MORA survey (C. M. Casey et al. 2021; J. A. Zavala et al. 2021), with $S_{\rm 2\,mm} = (0.48 \pm 0.13)$ mJy. We also fit the (sub)millimeter and far-infrared (FIR) photometry (including

Herschel; D. Lutz et al. 2011; S. J. Oliver et al. 2012) with the mmpz code (C. M. Casey 2020), determining that the probability of a redshift solution at $z < 5$ is lower than 9%, consistent with the spec-z measurement.

2.5. Radio Data for ERD-1

A radio detection at 3 GHz is available for ERD-1 from the VLA-COSMOS large program (V. Smolčić et al. 2017), with $S_{\rm 3\,GHz} = (11 \pm 2)$ μJy. ERD is not detected in the 1.4 GHz maps (E. Schinnerer et al. 2007), with $S_{\rm 1.4\,GHz} = (25 \pm 19)$ μJy or a 2σ limit of <63 μJy. This limit implies a radio slope $S \sim \nu^{\alpha}$ with $\alpha > -1.1$.

3. SED-fitting

We derive photometric redshifts with Eazy (G. B. Brammer et al. 2008) for both galaxies, using the standard set of templates tweak_fsps_QSF_12_v3 (C. Conroy & J. E. Gunn 2010) coupled with those generated by R. L. Larson et al. (2023), and by allowing the redshift to vary in the range [0, 10]. We independently estimate the photo-z and physical properties with Bagpipes (A. C. Carnall et al. 2018) using the stellar models from G. Bruzual & S. Charlot (2003), leaving the metallicity as a free parameter in the range [0.1, 1]$Z_{\odot}$, invoking a delayed exponentially declining star formation history (SFH) with a uniform prior on the e-folding time and on the total stellar mass formed in the ranges [0.3, 10] Gyr and [10^5, 10^{13}] $M_{\odot}$. Following M. Franco et al. (2023), we use a slightly different implementation of the SFH contained by default in Bagpipes, parameterizing the age of the main stellar population as a function of the Hubble time at a given redshift. We also add a recent instantaneous burst of star formation to the "secular" SFH taking place in the last t Myr, with a uniform prior on t and on the total stellar mass formed in the burst in the ranges [10, 100] and [0, 10^{13}] $M_{\odot}$. The synthetic SEDs by Bagpipes also include the emission lines modeled by Cloudy (G. J. Ferland et al. 2017) assuming a fixed ionization parameter of $\log(U) = -2$. To account for the possible dust emission that could be visible in the MIRI filter at high redshift, we also include the models by B. T. Draine & A. Li (2007) with uniform priors on the mass fraction of the polycyclic aromatic hydrocarbons ($q_{\rm PAH} \in [1, 4]$) and on the lower limit of starlight intensity distribution ($U_{\rm min} \in [0.1, 25]$). The γ factor is fixed at the value $\gamma = 0.02$. Finally, SEDs are dust-extincted assuming a D. Calzetti et al. (2000) law with a uniform prior on $A_{\rm v}$ in the range [0, 5] mag and a flat redshift prior from [0, 10].

As a final test, we explore the possible existence of biases due to the chosen parameterization of the SFH of Bagpipes invoking a nonparametric SFH with the continuity prior as prescribed by J. Leja et al. (2019). We compute the $\Delta \log(SFR)$ in six age bins (0–10, 10–25, 25–50, 50–100, 100–200, and 200–400 Myr) adopting a prior shaped as a t − distribution with $\sigma = 0.3$ and $\nu = 2$ degrees of freedom. All the other priors are the same as for the parametric SFH. The output is summarized in Table 1, while the best-fitting SEDs are shown in Figure 1. The inferred SFHs can be found in Figure 2.

3.1. Estimated Physical Properties

As seen in Figure 1, the two galaxies have similar best-fit SEDs, characterized by a red continuum with a Balmer break and strong emission lines. Indeed, a red continuum with Balmer break explains the high stellar masses and dust
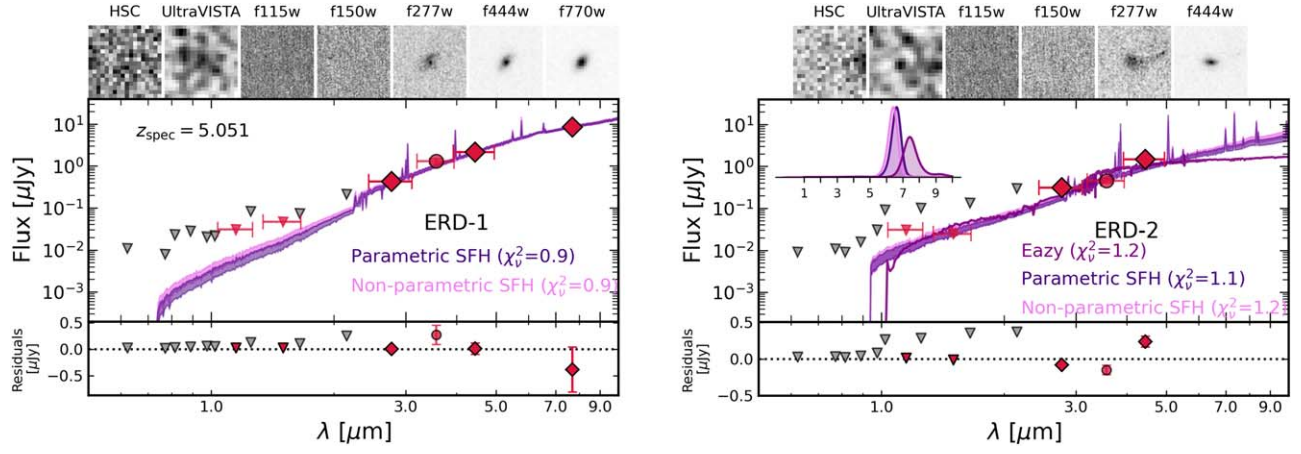
Figure 1. Cutouts (3″ × 3″) and best-fit spectral energy distributions for ERD-1 and ERD-2. Points have S/N > 3, while downward-pointing triangles represent 2σ upper limits. Photometry from JWST is in red, while other constraints are shown in gray. The first two cutout panels represent stacked images of the g, r, i, z, y bands of the HyperSupremeCam and the Y, J, H, Ks filters of the VISTA telescope, respectively. The inset on the right panel shows the redshift probability distributions for ERD-2 estimated by `Bagpipes` (with both SFHs) and `Eazy`. Shaded regions mark 16th–84th percentile confidence intervals on SED fits. The lower panels report the normalized residuals computed on the `Bagpipes` SED with parametric SFH.
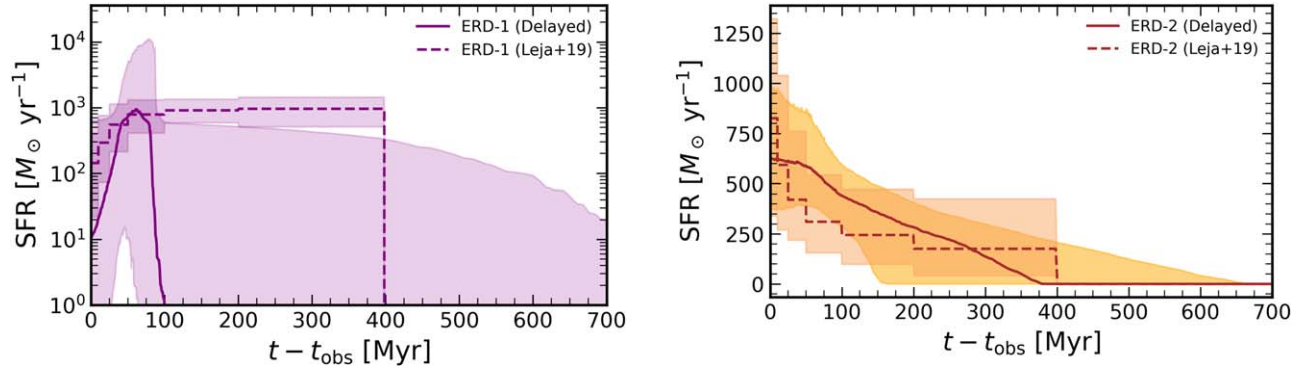

Figure 2. Star formation histories computed for our targets with `Bagpipes` by assuming a standard delayed exponentially declining SFH (solid lines) and the nonparametric one by J. Leja et al. (2019). In both panels, the shaded area reports the 16th–84th percentile of the posterior distribution.

Table 1
Properties of Our Galaxies Estimated through SED-fitting

Name	R.A. (J2000)	Decl. (J2000)	$z_{\rm spec}$ ...	$z_{\rm BG}^{\rm P}$ ...	$z_{\rm BG}^{\rm NP}$ ...	$z_{\rm EZ}$ ...	$\log(M_\star^{\rm P})$ $(M_\odot)$	$A_v^{\rm P}$ (mag)	$\log(M_\star^{\rm NP})$ $(M_\odot)$	$A_v^{\rm NP}$ (mag)
ERD-1	10:00:47.088	+02:10:16.680	5.051	$5.4^{+0.5}_{-0.4}$	$5.3^{+0.4}_{-0.4}$	$5.3^{+0.4}_{-0.4}$	$11.32^{+0.07}_{-0.15}$	$3.8^{+0.1}_{-0.2}$	$11.42^{+0.05}_{-0.07}$	$3.8^{+0.2}_{-0.2}$
ERD-2	10:01:07.368	+01:52:00.840	...	$6.7^{+0.3}_{-0.3}$	$6.6^{+0.2}_{-0.2}$	$7.3^{+0.3}_{-0.3}$	$11.2^{+0.1}_{-0.2}$	$2.9^{+0.3}_{-0.3}$	$11.0^{+0.1}_{-0.2}$	$3.0^{+0.2}_{-0.4}$

Note. The table reports, for each object, the two photometric redshifts computed by `Bagpipes` ($z_{\rm BG}$) and `Eazy` ($z_{\rm EZ}$). The stellar mass ($M_\star$) and dust attenuation (A_v) are estimated with `Bagpipes` with both a parametric (P) and nonparametric (NP) SFH.

extinction (because Balmer breaks imply older stellar populations that have a higher mass-to-light ratio). Moreover, the presence of strong emission lines suggests that these sources are actively forming stars. In addition, the presence of the Balmer break helps secure the photometric redshifts of our sources: the break between the Ks band and the F277W filter (for ERD-1) and between F277W and IRAC channel 1 (for ERD-2) produces the two photometric redshifts of $z \sim 5$ and $z \sim 6.5$ for the two galaxies, respectively.

As visible from Table 1, the photo-z estimated with `Eazy` and `Bagpipes` are in good agreement with each other (and, for ERD-1, just slightly higher than the spec-z measured by S. Jin et al. 2019, albeit compatible within the uncertainties). Since it is known, we fix the redshift of ERD-1 to the

spectroscopic redshift. Moreover, the physical properties estimated with the nonparametric SFH are in good agreement with those computed by assuming the more standard parametric SFH. In the following, we will assume the latter as reference values for both galaxies.

For ERD-1, we find a stellar mass of $\log(M_\star) = (11.32^{+0.07}_{-0.15})\,M_\odot$ and a dust attenuation of $A_v = (3.8^{+0.1}_{-0.2})$ mag. ERD-2 has $\log(M_\star) = (11.2^{+0.1}_{-0.2})\,M_\odot$ and $A_v = (2.9^{+0.3}_{-0.3})$ mag. The mass for ERD-1 is more accurate than that of ERD-2 thanks to the spec-z and the MIRI/F770W detection (tracing the rest-frame near-infrared wavelengths and—therefore—the bulk of the stellar mass, less affected by the presence of dust; see, e.g., C. Papovich et al. 2023; T. Wang et al. 2024c). The availability of a MIRI constraint for ERD-2 could, in principle, decrease the
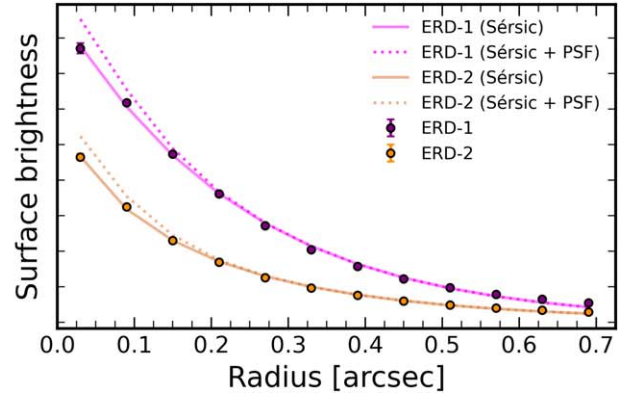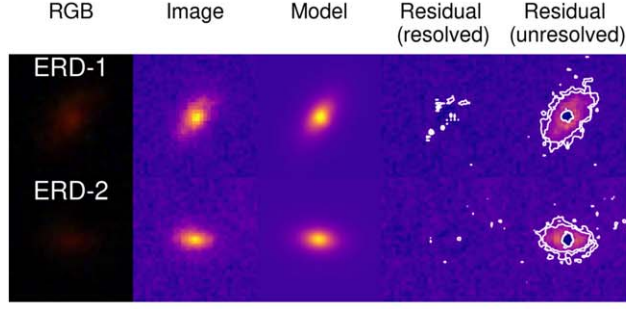
Figure 3. Left panel: Color-composite cutouts and F444W profile-fitting of ERD-1 and ERD-2 in $2'' \times 2''$ cutouts through `Imfit`. The last two panels show the residuals with the Sérsic model and an unresolved point source. We overplot the contours at 3σ and 5σ. A single Sérsic profile correctly reproduces the brightness profile of our objects without the need for an additional unresolved component. Right panel: surface brightness profile (in F444W) modeled with a single Sérsic profile and with the addition of an unresolved component. Again, the Sérsic profile well reproduces the observations.

inferred stellar mass. H. B. Akins et al. (2024) measure offset as high as ∼1 dex for LRDs with and without the additional MIRI point. However, this effect is primarily due to an overestimated age for the main stellar population (H. B. Akins et al. 2024). Since we find a young stellar population for ERD-2 ($\lesssim 400$ Myr; see Figure 2), we do not expect this effect to dramatically change our results. To better quantify this possibility, we run an additional test by artificially adding a MIRI/F770W point to the ERD-2 photometry and assuming a ratio [F770W]/[F444W] in the range [1,5], broadly consistent with measured LRD colors at similar redshifts (for instance, the same value for ERD-1 is ∼4). By again fitting the new photometry, we obtain a decrease of ∼0.4 dex in the inferred stellar mass with a completely flat SED. The offset rapidly decreases with higher F770W fluxes and becomes negligible with [F770W]/[F444W] ∼ 3. This result suggests that the 0.4 dex decrease should be interpreted as the maximum effect of the additional MIRI constraint on the stellar mass of ERD-2. Nevertheless, a MIRI follow-up of this galaxy would be crucial to properly estimate this value. Finally, following E. Daddi et al. (2010), we estimate the dynamical mass of ERD-1 from the FWHM of the CO line (∼850 km s^{-1}; S. Jin et al. 2019) and the physical size computed in Section 4). The obtained value of $\log(M_{\mathrm{Dyn}}) = (11.3 \pm 0.2) \, M_\odot$ is in good agreement with the inferred stellar mass.

Since neither galaxy is detected in F115W, we have a weak limit on the rest-frame UV flux. Hence, the values reported by the SED-fitting codes ($\log(\mathrm{SFR}) = 3.4^{+0.1}_{-0.6} \, M_\odot \, \mathrm{yr}^{-1}$ and $\log(\mathrm{SFR}) = 2.8^{+0.2}_{-0.2} \, M_\odot \, \mathrm{yr}^{-1}$ for ERD-1 and ERD-2, respectively) are largely unconstrained. However, since ERD-1 has multiple (sub)millimeter and radio detections—qualifying it for classic DSFGs selection (see, e.g., C. M. Casey et al. 2014)—and a spectroscopic redshift reducing the possible degeneracies, we estimate the obscured star formation rate (SFR). More specifically, by assuming a standard radio slope of $\alpha = -0.7$ (star-forming galaxies and in good agreement with the upper limit given in Section 2.5), we estimate a radio luminosity of $L_{1.4 \, \mathrm{GHz}} = (3.1 \pm 0.6) \times 10^{24} \, \mathrm{W} \, \mathrm{Hz}^{-1}$. Assuming that all the radio emission is produced by star formation, we use R. C. Kennicutt & N. J. Evans (2012) to estimate an $\mathrm{SFR}_{1.4 \, \mathrm{GHz}} = (1.6 \pm 0.3) \times 10^3 \, M_\odot \, \mathrm{yr}^{-1}$. This estimate is similar to that computed via the infrared SED in S. Jin et al. (2019): $L_{\mathrm{IR}} = (6 \pm 1) \times 10^{12} \, L_\odot$, implying an $\mathrm{SFR}_{\mathrm{IR}} = (1.0 \pm 0.3) \times 10^3 \, M_\odot \, \mathrm{yr}^{-1}$. We measure the FIR-to-radio luminosity ratio as $q_{\mathrm{IR}} = 2.3 \pm 0.2$ (see, e.g., G. Helou et al. 1985), in good

agreement with q_{IR} of star-forming galaxies (e.g., M. S. Yun et al. 2001). The high SFR also explains the presence of the strong nebular emission lines visible in the best-fit SEDs. All the abovementioned properties for ERD-1 suggest—together with the ALMA detections—that this galaxy belongs to the high-mass end of the dusty star-forming galaxy population (see, e.g., C. M. Casey et al. 2014; T. Wang et al. 2019; F. Gentile et al. 2024), something that is not always true of galaxies with red JWST colors (see, e.g., L. Barrufet et al. 2024).

4. Morphological Analysis

We use `Imfit` (P. Erwin 2015) to perform a two-dimensional profile fitting of our galaxies in F444W, the highest S/N filter, using a single Sérsic model, leaving the centroid, axis ratio, position angle, Sérsic index, effective radius, and flux as free parameters. Our resulting models describe the data well, with reduced $\chi^2 \sim 1$ (see Figure 3). From the profile fitting, we obtain that ERD-1 and ERD-2 have effective radii of (1.87 ± 0.02) kpc and (1.43 ± 0.02) kpc, respectively, and that both are well described by a Sérsic profile with $n \sim 1$.

We also fit the data to a combined model with both an unresolved point source and Sérsic profile. To limit the additional free parameters, we fix the unresolved centroid to the center of the Sérsic model, and leave the flux as a free parameter. The best-fitting model always converges toward a zero-flux point source. If we fix the contribution from the point source to be at least ∼20% of the total integrated flux (see, e.g., the right panel in Figure 3), we obtain a significantly worse fit, clearly indicating no contribution from an unresolved component.

5. Discussion

5.1. Estimating the Stellar Baryon Fraction

ΛCDM cosmology uniquely determines a certain mass function of dark matter halos at a given redshift (e.g., R. K. Sheth & G. Tormen 1999). However, converting this halo mass to a stellar mass is a more challenging task, since baryonic processes are complex and not completely understood, especially at high-z. Under the oversimplified hypothesis that all the baryons in halos are converted in stars (an assumption that is most certainly incorrect), we can derive a stringent upper limit on the galaxies' possible masses
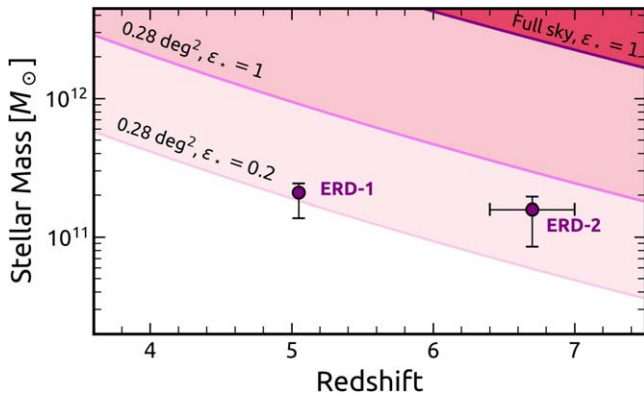
Figure 4. ERD-1 and ERD-2 in the stellar mass vs. redshift plane. The lines correspond to different number densities: 1.3×10^{-12} Mpc^{-3} (i.e., a single galaxy in the whole sky; dark violet) and 1.9×10^{-7} Mpc^{-3} (i.e., one source in the cosmic volume explored so-far by COSMOS-Web; dark red) with a (unrealistic) stellar baryon fraction of $\epsilon_\star = 1$. The lower (light pink) line scales down the second using a more reasonable efficiency of $\epsilon_\star = 0.2$.

at each redshift in a given cosmological volume (see, e.g., C. L. Steinhardt et al. 2016; P. Behroozi & J. Silk 2018; M. Boylan-Kolchin 2023) and compare our estimated stellar masses with these limits.

Here we follow the analysis of M. Boylan-Kolchin (2023).[24] We first consider the halo mass function by R. K. Sheth & G. Tormen (1999) and multiply it by the cosmic baryon fraction $f_b \sim 0.16$ (Planck Collaboration et al. 2020) to obtain a relationship between the maximal stellar mass and volume density: $M_\star = M_H f_b \epsilon_\star$. This value depends on $\epsilon_\star$, the stellar baryon fraction, describing the integrated history of the star formation efficiency in a given galaxy.

Considering the redshift range spanned by our galaxies ($5 < z < 7$) and the sky area analyzed here from COSMOS-Web (0.28 deg^2), we estimate that our survey covers a total comoving volume of 7.6×10^{11} Mpc^3. In Figure 4, we compare our sources' stellar masses with the maximum mass allowed with redshift in our survey volume. To fit within ΛCDM, the two galaxies presented in this Letter would require a (minimum) $\epsilon_\star = 0.24^{+0.02}_{-0.08}$ and $\epsilon_\star = 0.5^{+0.2}_{-0.2}$ (for ERD-1 and ERD-2, respectively) under the hypothesis that they are the only galaxies in the cosmic volume explored so far by COMSOS-Web with these masses at these redshifts.

5.2. Implication for Star Formation Efficiency

Star formation is known to be very inefficient, with several self-regulating processes limiting the efficiency at small scales (see, e.g., R. C. J. Kennicutt 1998; E. C. Ostriker & R. Shetty 2011). Observational studies at lower redshifts ($z \lesssim 2$–3) have an implied strong upper limit on $\epsilon_\star \ll 0.2$ (e.g., R. Mandelbaum et al. 2006; P. S. Behroozi et al. 2010; R. C. Kennicutt & N. J. Evans 2012; B. P. Moster et al. 2013; R. H. Wechsler & J. L. Tinker 2018; M. Shuntov et al. 2022), with some (e.g., P. S. Behroozi et al. 2010 and B. P. Moster et al. 2013) notably expecting a decreased integrated star formation efficiency toward higher redshifts and others finding a more constant behavior until at least $z \sim 4$ (e.g., P. S. Behroozi et al. 2013). Our values of $\epsilon_\star$ are significantly higher than these studies expect, suggesting star formation pathways much more efficient

at high-z than what is observed in the local Universe. This conclusion is strengthened by similar $\epsilon_\star$ reported by M. Xiao et al. (2023) for their red galaxy sample (with spectroscopic redshifts) from the FRESCO survey (P. A. Oesch et al. 2023), suggesting $\epsilon_\star \sim 0.5$, or with those reported by T. Wang et al. (2024c) for a sample of MIRI-detected massive galaxies, with a moderately lower $\epsilon_\star \sim 0.3$.

We underline, however, that the estimated $\epsilon_\star$ are also the product of some assumptions that—if proved wrong—could strongly affect the measured values. First, the halo mass function is a consequence of the assumed ΛCDM cosmology. Some alternative models (e.g., early dark energy; see, e.g., T. Karwal & M. Kamionkowski 2016; V. Poulin et al. 2018) forecast the early formation of more massive halos (e.g., A. Klypin et al. 2021). In this case, halos are more massive, and a larger baryonic mass would be available for star formation.

Second, the stellar masses obtained in this Letter assume a G. Chabrier (2003) IMF. Several works argue that this could be an oversimplification, due to the dependence of the IMF on the metallicity or the temperature of molecular clouds (see, e.g., C. Low & D. Lynden-Bell 1976; R. Dave 2008). A top-heavy IMF could produce lower stellar masses (with a factor $\gtrsim 0.3$ dex; see, e.g., C. Woodrum et al. 2023; B. Wang et al. 2024a) and give slightly lower values of $\epsilon_\star$.

Moreover, the possible contribution of reddened AGN emission to the continuum can significantly alter the stellar mass estimation (even with a spectroscopically confirmed Balmer break; see, e.g., B. Wang et al. 2024b). This hypothesis is ruled out for our galaxies thanks to their extended morphology, ensuring that the main contributor to the red continuum is the stellar emission.

Finally, even excluding the contribution of AGN, the presence of strong emission lines (due to intense star formation) can produce an overestimation of the stellar masses of galaxies (see, e.g., D. Schaerer & S. de Barros 2009). Unfortunately, the contribution of these lines is hard to constrain with photometry alone. Therefore, a spectroscopic follow-up with JWST would be necessary to further confirm the inferred physical properties of our targets.

While some simulations suggest that very efficient star formation may be possible in dense giant molecular clouds (e.g., P. Torrey et al. 2017; M. Y. Grudić et al. 2018; A. Dekel et al. 2023), the extended morphology in these cases seems somewhat disjointed from such an explanation. Further observations of the mass budget in such systems, e.g., from spatially resolved observations of [C II] dynamics from ALMA, may be crucial to deciphering the underlying puzzle.

6. Conclusions

In this Letter, we presented two candidate massive, extended, and highly dust-obscured galaxies: ERD-1 and ERD-2. These sources have extremely red (F277W–F444W ~ 1.7 mag) color, mimicking the selection of "little red dots" (e.g., H. B. Akins et al. 2023; G. Barro et al. 2023). However, these galaxies have an extended morphology, ruling out the possibility that the continuum is dominated by reddened nuclear activity (unlike the majority of LRDs), thus ensuring that the stellar emission is responsible for the observed red colors.

We have employed SED fitting using two different codes (`Eazy` and `Bagpipes`) yielding photo-z estimates of ERD-2 of $z \sim 6.7$, while a spec-z of 5.051 of ERD-1 (S. Jin et al. 2019)

---

[24] We use the github code referenced therein, provided at this link: https://github.com/mrbk/JWST_MstarDensity/tree/main.

is already published. Both the best-fitting SEDs show a red continuum with a Balmer break combined with emission lines. These features suggest a moderately aged stellar population with high stellar masses ($M_\star \sim 10^{11}\ M_\odot$) and dust extinction ($A_v > 2.5$ mag), together with an ongoing episode of significant star formation.

The high stellar masses, once placed in the cosmological context through comparison with the halo mass function, suggest that our galaxies could have a much higher stellar baryon fraction ($\epsilon_\star \gtrsim 0.2$) than what is commonly observed in lower-redshift sources.

Possible explanations of this result are a top-heavier IMF in the high-z Universe, a much more efficient star formation in the early stages of the cosmic history than has been constrained by observations at low-z, or an earlier formation of massive halos than what was predicted by ΛCDM.

These possible consequences increase the need for spectroscopic follow-up of these interesting systems, to confirm the photo-z (for ERD-2), confirm the presence of the Balmer breaks suggested by the photometry (e.g., B. Wang et al. 2024b), and to accurately measure the dynamical masses of our galaxies, which is fully possible using JWST directly or ALMA.

ORCID iDs

Fabrizio Gentile ● https://orcid.org/0000-0002-8008-9871
Caitlin M. Casey ● https://orcid.org/0000-0002-0930-6466
Hollis B. Akins ● https://orcid.org/0000-0003-3596-8794
Maximilien Franco ● https://orcid.org/0000-0002-3560-8599
Jed McKinney ● https://orcid.org/0000-0002-6149-8178
Edward Berman ● https://orcid.org/0000-0002-8494-3123
Olivia R. Cooper ● https://orcid.org/0000-0003-3881-1397
Nicole E. Drakos ● https://orcid.org/0000-0003-4761-2197
Michaela Hirschmann ● https://orcid.org/0000-0002-3301-3321
Arianna S. Long ● https://orcid.org/0000-0002-7530-8857
Georgios Magdis ● https://orcid.org/0000-0002-4872-2294
Anton M. Koekemoer ● https://orcid.org/0000-0002-6610-2048
Vasily Kokorev ● https://orcid.org/0000-0002-5588-9156
Marko Shuntov ● https://orcid.org/0000-0002-7087-0701
Margherita Talia ● https://orcid.org/0000-0003-4352-2063
Natalie Allen ● https://orcid.org/0000-0001-9610-7950
Santosh Harish ● https://orcid.org/0000-0003-0129-2079
Olivier Ilbert ● https://orcid.org/0000-0002-7303-4397
Henry Joy McCracken ● https://orcid.org/0000-0002-9489-7765
Jeyhan S. Kartaltepe ● https://orcid.org/0000-0001-9187-3605
Daizhong Liu ● https://orcid.org/0000-0001-9773-7479
Louise Paquereau ● https://orcid.org/0000-0003-2397-0360
Jason Rhodes ● https://orcid.org/0000-0002-4485-8549
Michael R. Rich ● https://orcid.org/0000-0003-0427-8387
Brant E. Robertson ● https://orcid.org/0000-0002-4271-0364
Sune Toft ● https://orcid.org/0000-0003-3631-7176
Ghassem Gozaliasl ● https://orcid.org/0000-0002-0236-919X

References

Aihara, H., AlSayyad, Y., Ando, M., et al. 2019, PASJ, 71, 114
Akins, H. B., Casey, C. M., Allen, N., et al. 2023, ApJ, 956, 61
Akins, H. B., Casey, C. M., Lambrides, E., et al. 2024, arXiv:2406.10341
Astropy Collaboration, Price-Whelan, A. M., Lim, P. L., et al. 2022, ApJ, 935, 167
Barro, G., Perez-Gonzalez, P. G., Kocevski, D. D., et al. 2023, ApJ, 963, 128, arXiv:2305.14418
Barrufet, L., Oesch, P., Marques-Chaves, R., et al. 2024, arXiv:2404.08052
Behroozi, P., & Silk, J. 2018, MNRAS, 477, 5382
Behroozi, P. S., Conroy, C., & Wechsler, R. H. 2010, ApJ, 717, 379
Behroozi, P. S., Wechsler, R. H., & Conroy, C. 2013, ApJL, 762, L31
Bertin, E. 2011, in ASP Conf. Ser. 442, Astronomical Data Analysis Software and Systems XX, ed. I. N. Evans et al. (ASP: San Francisco, CA), 435
Bertin, E., Schefer, M., Apostolakos, N., et al. 2020, in ASP Conf. Ser. 527, Astronomical Data Analysis Software and Systems XXIX, ed. R. Pizzo et al. (San Francisco, CA: ASP), 461
Bezanson, R., Labbe, I., Whitaker, K. E., et al. 2022, arXiv:2212.04026
Boylan-Kolchin, M. 2023, NatAs, 7, 731
Brammer, G. B., van Dokkum, P. G., & Coppi, P. 2008, ApJ, 686, 1503
Bruzual, G., & Charlot, S. 2003, MNRAS, 344, 1000
Calzetti, D., Armus, L., Bohlin, R. C., et al. 2000, ApJ, 533, 682
Carnall, A. C., McLure, R. J., Dunlop, J. S., & Dave, R. 2018, MNRAS, 480, 4379
Casey, C. M. 2020, ApJ, 900, 68
Casey, C. M., Akins, H. B., Shuntov, M., et al. 2024, ApJ, 965, 98
Casey, C. M., Kartaltepe, J. S., Drakos, N. E., et al. 2023, ApJ, 954, 31
Casey, C. M., Narayanan, D., & Cooray, A. 2014, PhR, 541, 45
Casey, C. M., Zavala, J. A., Manning, S. M., et al. 2021, ApJ, 923, 215
Chabrier, G. 2003, PASP, 115, 763
Conroy, C., & Gunn, J. E. 2010, ApJ, 712, 833
Daddi, E., Bournaud, F., Walter, F., et al. 2010, ApJ, 713, 686
Dave, R. 2008, MNRAS, 385, 147
Dekel, A., Sarkar, K. C., Birnboim, Y., Mandelker, N., & Li, Z. 2023, MNRAS, 523, 3201
Draine, B. T., & Li, A. 2007, ApJ, 657, 810
Erwin, P. 2015, ApJ, 799, 226
Ferland, G. J., Chatzikos, M., Guzmán, F., et al. 2017, RMxAA, 53, 385
Finkelstein, S. L., Bagley, M. B., Ferguson, H. C., et al. 2023, ApJL, 946, L13
Franco, M., Akins, H. B., Casey, C. M., et al. 2023, arXiv:2308.00751
Furtak, L. J., Labbé, I., Zitrin, A., et al. 2024, Nature, 628, 57
Gentile, F., Talia, M., Behiri, M., et al. 2024, ApJ, 962, 26
Greene, J. E., Labbe, I., Goulding, A. D., et al. 2024, ApJ, 964, 39

Grudić, M. Y., Hopkins, P. F., Faucher-Giguère, C.-A., et al. 2018, MNRAS, 475, 3511

Helou, G., Soifer, B. T., & Rowan-Robinson, M. 1985, ApJL, 298, L7

Jin, S., Daddi, E., Magdis, G. E., et al. 2019, ApJ, 887, 144

Karwal, T., & Kamionkowski, M. 2016, PhRvD, 94, 103523

Kennicutt, R. C. J. 1998, ARA&A, 36, 189

Kennicutt, R. C., & Evans, N. J. 2012, ARA&A, 50, 531

Klypin, A., Poulin, V., Prada, F., et al. 2021, MNRAS, 504, 769

Kocevski, D. D., Onoue, M., Inayoshi, K., et al. 2023, ApJL, 954, L4

Koekemoer, A. M., Aussel, H., Calzetti, D., et al. 2007, ApJS, 172, 196

Kokorev, V., Caputi, K. I., Greene, J. E., et al. 2024, ApJ, 968, 38

Kümmel, M., Bertin, E., Schefer, M., et al. 2020, in ASP Conf. Seri. 527, Astronomical Data Analysis Software and Systems XXIX, ed. R. Pizzo et al. (San Francisco, CA: ASP), 29

Labbé, I., Greene, J. E., Bezanson, R., et al. 2023b, arXiv:2306.07320

Labbé, I., van Dokkum, P., Nelson, E., et al. 2023a, Natur, 616, 266

Larson, R. L., Hutchison, T. A., Bagley, M., et al. 2023, ApJ, 958, 141

Leja, J., Carnall, A. C., Johnson, B. D., Conroy, C., & Speagle, J. S. 2019, ApJ, 876, 3

Low, C., & Lynden-Bell, D. 1976, MNRAS, 176, 367

Lutz, D., Poglitsch, A., Altieri, B., et al. 2011, A&A, 532, A90

Mandelbaum, R., Seljak, U., Kauffmann, G., Hirata, C. M., & Brinkmann, J. 2006, MNRAS, 368, 715

Matthee, J., Naidu, R. P., Brammer, G., et al. 2024, ApJ, 963, 129

McCracken, H. J., Milvang-Jensen, B., Dunlop, J., et al. 2012, A&A, 544, A156

Moneti, A., , Euclid Collaboration, Euclid Collaboration, McCracken, H. J., et al. 2022, A&A, 658, A126

Moster, B. P., Naab, T., & White, S. D. M. 2013, MNRAS, 428, 3121

Oesch, P. A., Brammer, G., Naidu, R. P., et al. 2023, MNRAS, 525, 2864

Oke, J. B., & Gunn, J. E. 1983, ApJ, 266, 713

Oliver, S. J., Bock, J., Altieri, B., et al. 2012, MNRAS, 424, 1614

Ostriker, E. C., & Shetty, R. 2011, ApJ, 731, 41

Papovich, C., Cole, J. W., Yang, G., et al. 2023, ApJL, 949, L18

Pérez-González, P. G., Barro, G., Rieke, G. H., et al. 2024, ApJ, 968, 4

Planck Collaboration, Aghanim, N., Akrami, Y., et al. 2020, A&A, 641, A6

Poulin, V., Boddy, K. K., Bird, S., & Kamionkowski, M. 2018, PhRvD, 97, 123504

Schaerer, D., & de Barros, S. 2009, A&A, 502, 423

Schinnerer, E., Smolčić, V., Carilli, C. L., et al. 2007, ApJS, 172, 46

Scoville, N., Aussel, H., Brusa, M., et al. 2007, ApJS, 172, 1

Sérsic, J. L. 1963, BAAA, 6, 41

Shen, X., Hopkins, P. F., Faucher-Giguère, C.-A., et al. 2020, MNRAS, 495, 3252

Sheth, R. K., & Tormen, G. 1999, MNRAS, 308, 119

Shuntov, M., McCracken, H. J., Gavazzi, R., et al. 2022, A&A, 664, A61

Smolčić, V., Novak, M., Bondi, M., et al. 2017, A&A, 602, A1

Steinhardt, C. L., Capak, P., Masters, D., & Speagle, J. S. 2016, ApJ, 824, 21

Szalay, A. S., Connolly, A. J., & Szokoly, G. P. 1999, AJ, 117, 68

Torrey, P., Hopkins, P. F., Faucher-Giguère, C.-A., et al. 2017, MNRAS, 467, 2301

Wang, B., de Graaff, A., Davies, R. L., et al. 2024b, arXiv:2403.02304

Wang, B., Leja, J., Atek, H., et al. 2024a, ApJ, 963, 74

Wang, T., Schreiber, C., Elbaz, D., et al. 2019, Natur, 572, 211

Wang, T., Sun, H., Zhou, L., et al. 2024c, arXiv:2403.02399

Weaver, J. R., Kauffmann, O. B., Ilbert, O., et al. 2022, ApJS, 258, 11

Wechsler, R. H., & Tinker, J. L. 2018, ARA&A, 56, 435

Williams, C. C., Alberts, S., Ji, Z., et al. 2024, ApJ, 968, 34

Woodrum, C., Rieke, M., Ji, Z., et al. 2023, arXiv:2310.18464

Xiao, M., Oesch, P., Elbaz, D., et al. 2023, arXiv:2309.02492

Yun, M. S., Reddy, N. A., & Condon, J. J. 2001, ApJ, 554, 803

Zavala, J. A., Casey, C. M., Manning, S. M., et al. 2021, ApJ, 909, 165